JOURNAL OF MATERIALS SCIENCE 24 (1989) 1845–1852

Effect of long-range ordering on the corrosion properties of an Ni–Mo alloy

H. M. TAWANCY, N. M. ABBAS
Central Analytical and Materials Characterization Laboratories, Metrology, Standards and Materials Division, Research Institute, King Fahd University of Petroleum and Minerals, Dhahran 31261, Saudi Arabia

A correlation was made between long-range ordering to Ni_4Mo ($A_4 \rightarrow D1_a$ superlattice) in a Ni–28wt% Mo alloy and its corrosion properties. Emphasis was placed upon the effects of ordering on: (i) microchemical composition including grain-boundary chemistry, and (ii) plastic deformation behaviour. Analytical electron microscopy and Auger electron spectroscopy were utilized for microstructural characterization and microchemical analysis. Corrosion testing in the ordered state revealed a considerable increase in the corrosion rate in boiling 20% HCl and also less resistance to stress corrosion cracking in boiling 10% HI, all relative to the disordered state. Molybdenum-depleted zones were detected in the ordered microstructure near the Ni_4Mo–matrix interfaces, at antiphase boundaries and alongside grain boundaries. Examination of the tensile deformation substructure indicated that ordering had lowered the stacking-fault energy of the alloy. It was concluded that the observed degradation in the chemical stability of the alloy in the ordered state was due to inhomogeneities in microchemical composition and a low stacking-fault energy.

1. Introduction

Nickel-base alloys have been of particular importance to the chemical process, petrochemical and oil industries because of their unique combinations of corrosion resistance, mechanical strength and fabrication characteristics [1]. Alloying with molybdenum is known to be essential for corrosion resistance in reducing media and also for resistance to localized corrosion [2]. Characteristic corrosion resistance of an alloy is obtained when the concentration of the noble metal, in this case molybdenum, is above a critical value known as the "reaction limit". Ni–Mo alloys containing 20 to 30 wt % Mo are the basis for the commercial Hastelloy® (Haynes International) B/B-2 type alloys which are characterized by excellent corrosion resistance to HCl at all temperatures and concentrations [1]. Alloy B-2, in particular, is also resistant to grain-boundary precipitation of molybdenum-rich carbides in a weld heat-affected zone which makes it suitable for most chemical process applications in the as-welded condition [3].

In recent years, ordered alloys and intermetallic compounds have attracted considerable attention because of their potential in structural high-temperature and corrosion applications [4, 5]. Most emphasis, however, has been placed upon understanding the effect of ordering on mechanical strength and identifying means of improving the ductility. It is equally important to characterize the effect of long-range ordering on the corrosion properties particularly in those alloys which have potential corrosion applications.

To demonstrate this effect, alloy B-2 was selected for this study because it is known to undergo a long-range ordering reaction upon exposure to temperatures in the range of 600 to 800° C, whereby disordered fcc lattice → ordered Ni_4Mo (tetragonal, $D1_a$ superlattice) [6]. Table I gives the nominal chemical composition of alloy B-2. Earlier investigations of long-range ordering to Ni_4Mo in this alloy showed that both a $D0_{22}$ superlattice (Ni_3Mo composition) and a Pt_2Mo-type superlattice (Ni_2Mo composition) form as metastable transient phases [7, 8]. Crystallographically, the $D1_a$, $D0_{22}$ and Pt_2Mo-type superlattices are closely related in that they can all, directly, be derived from the parent fcc lattice by atom rearrangements on the $\{420\}_{fcc}$ planes (All subsequent crystallographic notations are given in terms of fcc lattice). In the case of the $D1_a$ superlattice, every fifth plane is occupied by molybdenum atoms and planes in between contain only nickel atoms, thus there are six crystallographically equivalent variations of Ni_4Mo. For the $D0_{22}$ and Pt_2Mo-type superlattices, the molybdenum atoms occupy, respectively, every fourth and third plane. Thus, in electron diffraction

TABLE I Nominal chemical composition of alloy B-2 (wt %)

Ni	Balance
Mo	26–30
Fe	2.0*
Cr	1.0*
Co	1.0*
Mn	1.0*
Si	0.1*
C	0.1*

*Maximum

0022-2461/89 $03.00 + .12

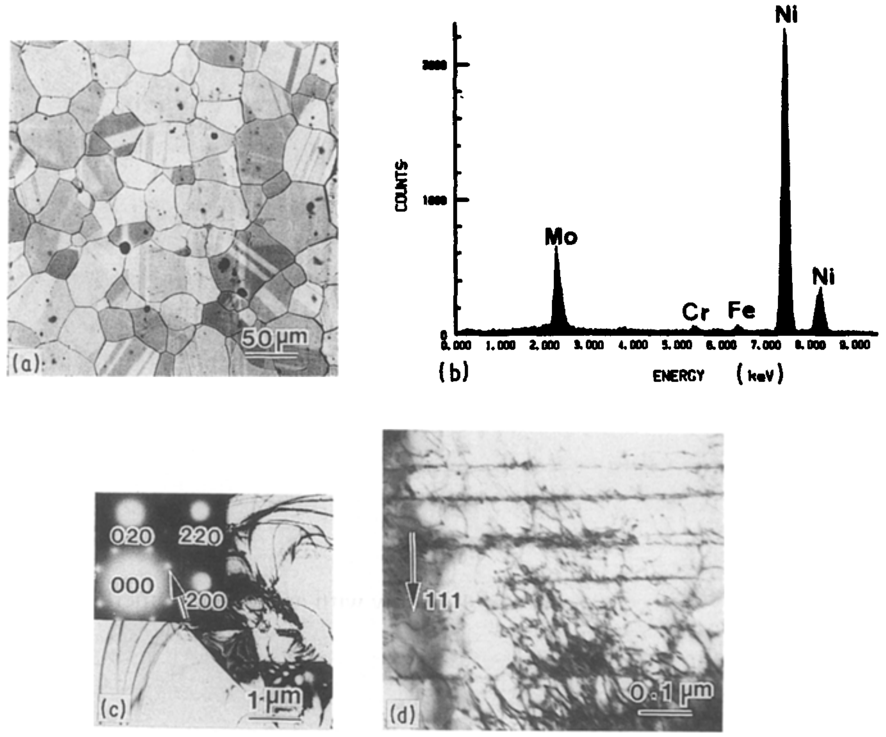

Figure 1 Characteristic microstructural features of alloy B-2 in the annealed condition (disordered). (a) Back-scattered electron composition image illustrating a typical grain structure. (b) EDS spectrum derived from point analysis of the alloy's chemistry (see Table II). (c) Bright-field TEM image and corresponding SAD pattern in [0 0 1] orientation showing short-range order reflections at $\{1\frac{1}{2}0\}$ positions, (arrowed). (d) Bright-field TEM image illustrating dislocation structure in a specimen given 3% elongation.

patterns, the characteristic reflections of the $D1_a$, $D0_{22}$ and Pt_2Mo-type superlattices appear, respectively, at $\frac{1}{5}\langle 420\rangle$, $\frac{1}{4}\langle 420\rangle$ and $\frac{1}{3}\langle 420\rangle$ positions and all equivalent positions.

It was the objective of this investigation to establish the relationship between long-range ordering to Ni_4Mo in alloy B-2 and its corrosion properties with reference to the effect of ordering on (i) microchemical composition of the matrix and grain-boundary chemistry, and (ii) plastic deformation behaviour.

2. Experimental procedure

Sheet samples about 1 mm thick of a commercial grade heat of alloy B-2 were provided by Haynes International. All specimens were first annealed at 1065° C and then water quenched. To induce long-range ordering, specimens were aged at temperatures in the range of 500 to 900° C and finally air-cooled. Microstructural characterization and microchemical analysis were performed in an analytical electron microscope and a scanning Auger microprobe. Thin foils were examined in the transmission electron microscopy (TEM), scanning transmission electron microscopy (STEM) and high resolution lattice imaging modes at an accelerating voltage of 200 kV and bulk samples were examined in the scanning electron microscopy (SEM) mode at 25 kV. A jet polisher was used to prepare thin foils in a solution of 30% nitric acid in methanol kept at about $-20°$ C.

In certain ordered states, the tensile fracture mode was predominantly intergranular; therefore, selected specimens were *in situ* fractured in a scanning Auger microprobe and then sputtered at a rate of 1 nm min^{-1} to generate depth profiles for molybdenum, i.e. concentration compared to distance from grain boundary. Corrosion properties were determined from aqueous corrosion tests in boiling 20% HCl and stress corrosion cracking tests in boiling 10% HI. Aqueous corrosion rates were calculated from width loss measurements made on 25.4 mm × 25.4 mm × 1.0 mm specimens after 24 h immersion in HCl. Stress corrosion cracking tests were conducted on flat specimens (45.0 mm × 4.5 mm × 1.0 mm) which were strained as C-shape to a final length of 39 mm and then held at a constant plastic strain in slotted holders having 50 mm × 50 mm × 6 mm overall dimensions. Resistance to stress corrosion cracking was taken as the number of specimens cracked out of number of specimens tested. Room-temperature tensile tests were conducted on specimens having a gauge length of 25.4 mm.

TABLE II Characteristic properties in the disordered state (annealed, 1065° C/15 min/water quenching)

Room-temperature tensile properties	
0.2% Yield strength, MPa (10^3 psi)	415 (60)
Ultimate tensile strength, MPA (10^3 psi)	880 (127.5)
Tensile elongation in 25.4 mm (2 in.), %	76
Corrosion properties	
Corrosion rate in boiling 20% HCl (24 h immersion test), mm^{-1} y (mils/year)	0.2 (9.3)
Stress corrosion cracking resistance, (100 h exposure; boiling 10% HI), number of specimens cracked/number of specimens tested	no cracking

3. Results and discussion

3.1. Characterization of annealed material (disordered)

Table II summarizes the aqueous corrosion rate in boiling 20% HCl, resistance to stress corrosion cracking in boiling 10% HI and room-temperature tensile properties in the annealed condition (1065° C/15 min/water quenching). Corresponding microstructural features are illustrated in Fig. 1. A typical grain structure is shown in the back-scattered electron

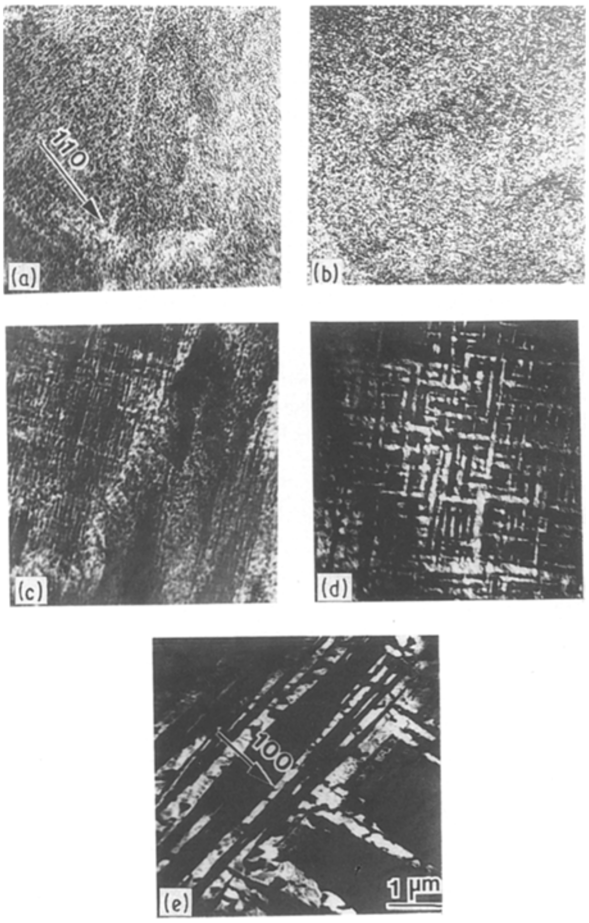

Figure 2 A set of dark-field TEM images formed with $\frac{1}{5}\langle 420\rangle$ characteristic Ni_4Mo reflections to illustrate the evolution of the ordered microstructure during ageing at 700° C. Aged (a) 15 min, (b) 2 h, (c) 8 h, (d) 24 h, (e) 100 h.

composition image of Fig. 1a. Full recrystallization was indicated by the presence of a high density of annealing twins. An example of energy dispersive X-ray spectroscopy (EDS) performed in the SEM mode to characterize the alloy's chemistry is given in Fig. 1b. Table III compares the results of wet chemical analysis and quantitative analysis of the spectral data in Fig. 1b. Fig. 1c shows a bright-field TEM image and its corresponding selected-area diffraction (SAD) pattern in [0 0 1] orientation. Weak reflections can be seen at $\{1\frac{1}{2}0\}$ positions which characterize short-range order in Ni–Mo alloys, e.g. [9].

It is qualitatively known that alloys having low stacking fault energy [10] and/or containing short-range order [11] are the most susceptible to stress corrosion cracking. Presumably, coplanar groupings of dislocations promoted by a low stacking-fault energy and/or short-range order provide preferred sites for corrosion attack [10, 11]. Examination of the tensile deformation substructure in the annealed condition (disordered) showed the absence of cellular dislocation structure; however, the observation of coplanar groupings of dislocations with evidence of cross-slip (Fig. 1d) indicated a medium stacking-fault energy [12]. It is shown later that long-range ordering in the alloy investigated had the effect of lowering its stacking-fault energy with an attendant increase in its susceptibility to stress corrosion cracking.

TABLE III Chemical analysis of the heat investigated (wt %)

	Wet analysis	EDS analysis (Fig. 1b)
Ni	70.12	70.72
Mo	27.35	27.88
Fe	1.04	0.83
Cr	0.82	0.57

3.2. Evolution of the ordered microstructure

A set of dark-field TEM images formed with characteristic $D1_a$ superlattice reflections at $\frac{1}{5}\langle 420\rangle$ which illustrate the evolution of the ordered microstructure of Ni_4Mo during ageing at 700° C is shown in Fig. 2. In the early stages of ordering, a "tweed" contrast comprised of fine striations lying along traces of the $\{1\,1\,0\}$ planes was observed as shown in Fig. 2a. Such a contrast could arise from a non-random high-density distribution of tetragonal strain centres in the parent cubic lattice [13]. Subsequently, the tweed contrast was replaced by aligned arrays of discrete particles (Fig. 2b) which then grew to impingement (Fig. 2c) and produced a mosaic assembly of transformation twins (Fig. 2d) which continued to grow with ageing (Fig. 2e). Fig. 3 illustrates the twin relationship between two variants of Ni_4Mo with $\langle 1\,0\,0\rangle$ as a twin-axis. In addition to transformation twins (Fig. 3), the defect structure produced by the ordering reaction included: (i) antiphase boundaries parallel to $\{4\,2\,0\}$ planes, and (ii) micro-twins and stacking faults on $\{1\,1\,1)$ planes as summarized in Fig. 4. It is believed that both the micro-twins and stacking faults formed to accommodate the transformation strain which indicated a lower stacking fault energy in the ordered state as discussed further later.

Heterogeneous ordering was observed to occur at the grain boundaries by a discontinuous mechanism

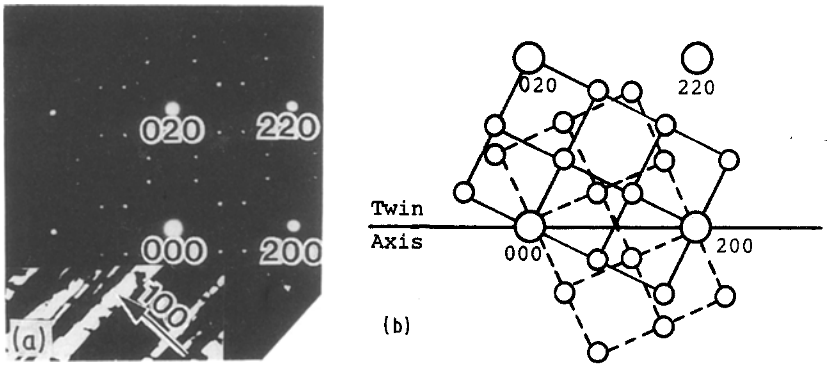

Figure 3 An illustration of the twin relationship between two variants of Ni_4Mo. (a) [0 0 1] SAD pattern and a dark-field image formed with a $\frac{1}{5}\langle 420\rangle$ reflection showing two twin-related variants of Ni_4Mo. (b) Interpretation of the SAD pattern in (a) as two twin-related patterns with $\langle 1\,0\,0\rangle$ as a twin-axis.

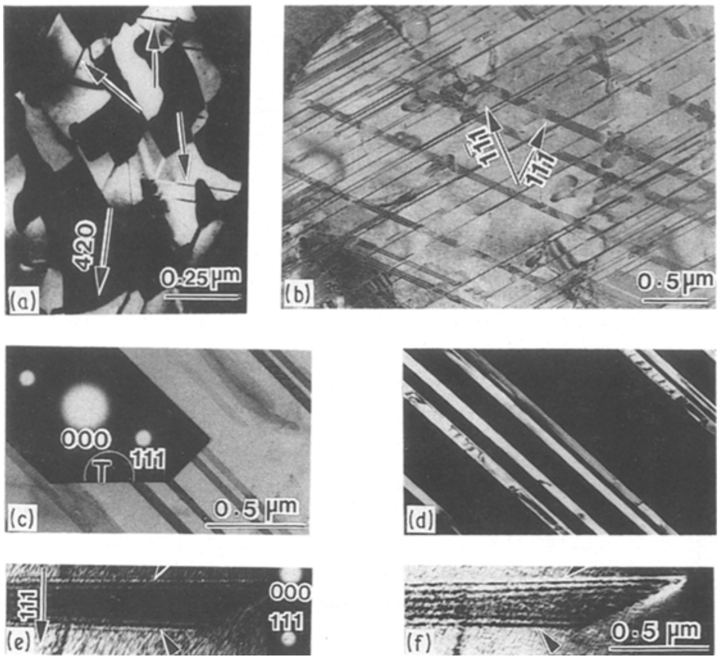

Figure 4 Defect structure produced by long-range ordering to Ni_4Mo. (a) Dark-field TEM image formed with $\frac{1}{5}\langle 420\rangle$ reflection illustrating antiphase boundaries parallel to $\{420\}$ planes. (b) Bright-field TEM image showing a mixture of micro-twins and stacking faults on $\{111\}$ planes. (c), (d) Identification of micro-twins; (c) is a bright-field TEM image of micro-twins and corresponding twin pattern near [1 1 0] orientation, and (d) is a dark-field TEM image formed with the twin reflection marked T in (c). (e), (f) Identification of stacking faults; (e) is a bright-field TEM image and corresponding SAD pattern in two-beam condition ($g \equiv \langle 111\rangle$), and (f) is a dark-field TEM image formed with the (1 1 1) reflection in (e), note the symmetry and asymmetry of the outer-most fringes in bright- and dark-field images, respectively, which characterize a stacking fault.

which resulted in a lamellar morphology of Ni_4Mo as illustrated in Fig. 5. As would be expected from a consideration of the rate-determining factors, heterogeneous ordering at the grain boundaries was more pronounced either after relatively short ageing times at lower temperatures or after longer ageing times at higher temperatures, e.g. after 100 h at 700° C as in the example of Fig. 5.

3.3. Effect of ordering on microchemical composition

As indicated earlier, both $D0_{22}$ and Pt_2Mo-type superlattices were observed to form as transient metastable phases during long-range ordering to Ni_4Mo in the alloy investigated [7, 8]. An example illustrating the co-existence of $D0_{22}$ and $D1_a$ superlattices after 24 h of ageing at 700° C is given in Fig. 6. Characteristic $D0_{22}$ superlattice reflections can be observed at $\{100\}$, $\{1\frac{1}{2}0\}$ and $\{110\}$ positions in addition to $D1_a$ superlattice reflections at $\frac{1}{5}\langle 420\rangle$ positions. It is to be noted that the $D0_{22}$ superlattice has the Ni_3Mo composition. This observation demonstrated one type of inhomogeneity in microchemical composition which could occur during long-range ordering to Ni_4Mo.

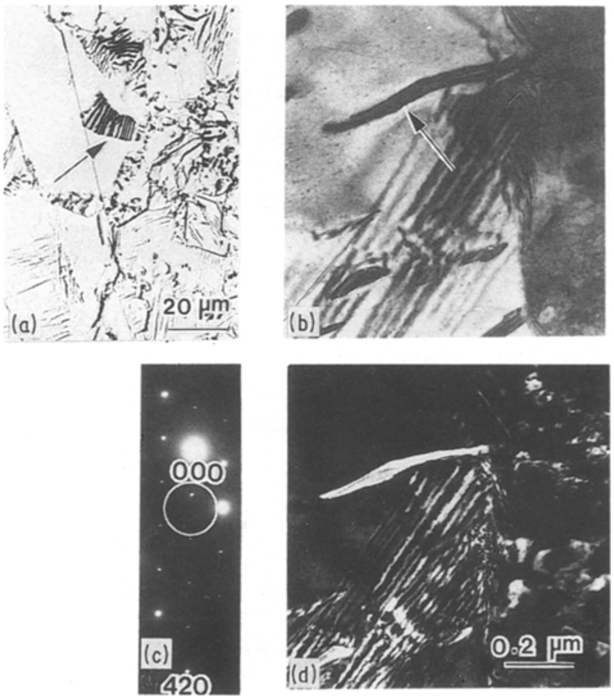

Figure 5 Discontinuous ordering to Ni_4Mo at a grain boundary (specimen aged 100 h at 700° C). (a) Light optical micrograph illustrating lamellar structure of Ni_4Mo at grain boundaries. (b) Bright-field TEM image of Ni_4Mo lamella at a grain boundary. (c) SAD pattern corresponding to (b) showing Ni_4Mo reflections at $\frac{1}{5}\langle 420\rangle$ positions. (d) Dark-field TEM image of the lamella in (b) formed with the encircled reflection in (c).

Another type of inhomogeneity was observed at antiphase boundaries of Ni_4Mo as illustrated in the high resolution one-dimensional lattice image of $\{420\}$ planes derived from a specimen aged 8 h at 700° C and is shown in Fig. 7. Similar to an earlier observation of $\{420\}$ lattice image in a binary Ni–Mo alloy [14], the crystal on one side of the boundary in Fig. 7 is shifted by two fundamental lattice planes, i.e. two-fifths of the superlattice spacing, relative to the crystal on the other side. A close examination of the fringe pattern in Fig. 7 revealed that the local composition at the boundary is Ni_5Mo, i.e. the antiphase boundary is of the non-conservative type. Also, inhomogeneities in microchemical composition were observed near the Ni_4Mo–matrix interfaces. An example is illustrated in Fig. 8 which shows a STEM image of Ni_4Mo particles in a specimen aged 8 h at 700° C and corresponding EDS spectra derived from Ni_4Mo and the adjacent matrix as indicated in Fig. 8a. Table IV summarizes the results of standardless quantitative analysis of the spectral data of Figs 8b, c performed by a software based upon the thin-film

TABLE IV Results of quantitative analysis of the spectral data in Fig. 8 (wt %)

	Ni_4Mo (Fig. 8a)	Adjacent matrix (Fig. 8b)
Ni	70.63	92.02
Mo	29.37	6.54
Fe	–	0.83
Cr	–	0.61

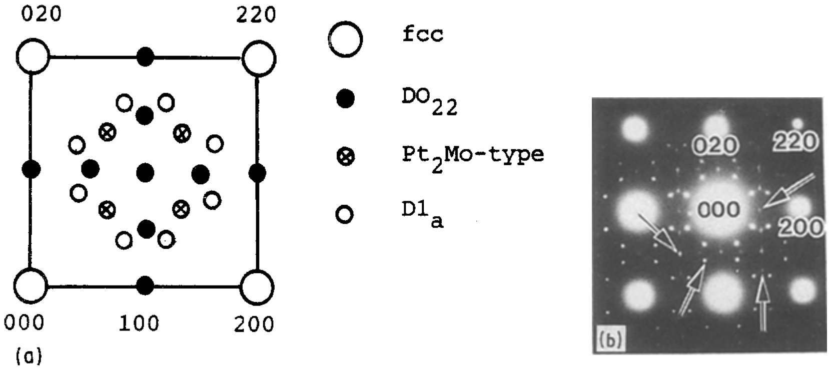

Figure 6 An example illustrating the co-existence of $D1_a$ and $D0_{22}$ superlattices in a specimen aged 24 h at 700° C. (a) A schematic illustration of [0 0 1] reciprocal lattice intersection illustrating the relative positions of the $D1_a$, $D0_{22}$ and Pt_2Mo-type superlattices with respect to those of the parent fcc lattice. (b) SAD pattern in [0 0 1] orientation illustrating the formation of a $D0_{22}$ superlattice during long-range ordering to Ni_4Mo.

approximation [15]. As illustrated in Table IV, the molybdenum content of Ni_4Mo was observed to be 29.37 wt % which is in excellent agreement with that characteristic of the stoichiometric composition (29.1 wt %). A considerable depletion in molybdenum was, however, observed near the Ni_4Mo–matrix interface as illustrated in Fig. 8 and Table IV. Such a depletion could result from the difficulty to reestablish equilibrium composition near the interface because of the low diffusivity of molybdenum in nickel.

Molybdenum-depleted zones were also observed alongside grain boundaries by Auger electron spectroscopy as shown in the example of Fig. 9 for a specimen aged 100 h at 700° C. In that condition, the room-temperature tensile ductility was 3%. As shown in the inset of Fig. 9, the surface of as-fractured specimen in a scanning Auger microprobe, exhibited a predominantly intergranular fracture mode. Analysis of the molybdenum concentration in the as-fractured condition and during sputtering of a 27 nm layer, resulted in the profile shown in Fig. 9. Depletion of molybdenum alongside the grain boundaries could result from the discontinuous ordering reaction described earlier (Fig. 5).

The above observations demonstrated that long-range ordering to Ni_4Mo in the alloy investigated led to inhomogeneities in microchemical composition which appeared in the form of molybdenum-depleted zones both in the matrix and alongside grain boundaries. As shown later, these inhomogeneities were found to degrade the chemical stability of the alloy in a reducing medium such as HCl.

3.4. Plastic deformation behaviour in the ordered state

Fig. 10 illustrates true tensile stress–strain curves derived at room temperature from specimens in the following conditions: (a) disordered (annealed), (b) ordered to discrete particles of Ni_4Mo (aged 2 h at 700° C, Fig. 2b), and (c) ordered to platelets of Ni_4Mo (aged 100 h at 700° C Fig. 2e). It is evident from Fig. 10 that ordering had caused considerable increase in tensile strength and decrease in tensile ductility. However, it is to be noted that a relatively high ductility level (~ 30% elongation) was maintained when the alloy was ordered to discrete particles of Ni_4Mo (curve b, Fig. 10). When the morphology changed to platelet-type (curve c, Fig. 10), almost complete loss of ductility occurred although there was no significant change in the degree of order as determined from X-ray diffraction. This behaviour could be interpreted in terms of the easy crack propagation paths provided by platelets of Ni_4Mo. Typical tensile deformation substructures and corresponding fracture surfaces in the ordered state are illustrated in Fig. 11. Twinning on the $\{1\,1\,1\}$ planes was the predominant deformation mode when Ni_4Mo assumed a discrete-particle morphology as shown in Fig. 11a. In this case, tensile fracture occurred by a transgranular mode (dimple-type rupture) which is typical of a ductile material (Fig. 11b). When Ni_4Mo assumed a platelet-type morphology, a high density of $\{1\,1\,1\}$ stacking faults was observed in the deformation substructure (Fig. 11d). Recognizing that a stacking fault is a thin layer of a twin, it is possible that the easy crack propagation paths provided by the platelet-type morphology caused fracture to occur before stacking faults (Fig. 11c) could grow into twins and contribute to macroscopic strain. Long-range ordering to Ni_4Mo in a binary Ni–Mo alloy was also found to lower its stacking-fault energy [16].

TABLE V Stress corrosion cracking resistance in the ordered state (100 h exposure: boiling 10% HI)

Condition	Number of specimens cracked/ number of specimens tested
Aged 2 h at 700° C	2/2
Aged 100 h at 700° C	2/2

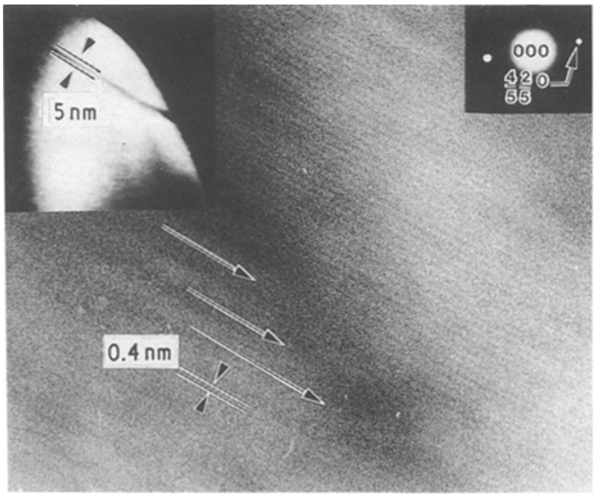

Figure 7 High-resolution lattice image of $\{4\,2\,0\}$ planes in a specimen aged 8 h at 700° C showing an antiphase boundary (arrowed). The insets show a dark-field image of the boundary and the diffraction condition utilized in forming the image.

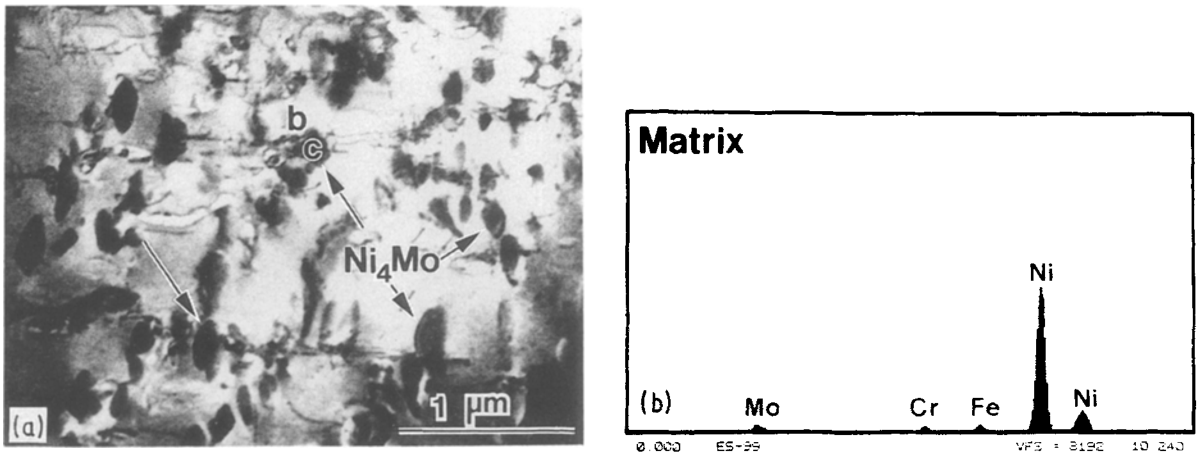

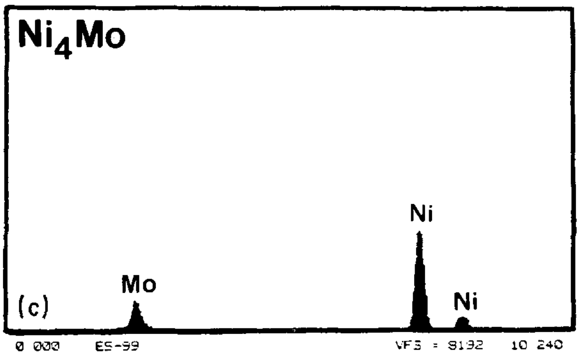

Figure 8 A STEM experiment demonstrating the presence of a molybdenum-depleted zone near Ni_4Mo particle–matrix interface. (a) Bright-field STEM image of Ni_4Mo particles in a specimen aged 8 h at 700° C. (b) EDS spectrum derived in the STEM mode from the matrix point marked b in (a). (c) EDS spectrum derived in the STEM mode from the Ni_4Mo particle marked c in (a), see Table IV.

It could be concluded from the above observations that the ordering reaction had the effect of lowering the stacking-fault energy of the alloy and as a result it would be expected to become more susceptible to stress corrosion cracking as shown below.

3.5. Effect of ordering on corrosion properties

Fig. 12 summarizes the effects of ageing temperatures (500 to 900° C) and times at a temperature (15 min to 2 h) on the corrosion rate in boiling 20% HCl. A considerable increase in the corrosion rate can be seen to have occurred after ageing at 600 to 800° C which coincided with the occurrence of long-range ordering. Noting that the boiling reducing acid corrosion test (HCl) detects molybdenum-depleted zones, the observed increase in corrosion rate (Fig. 12) could be correlated with the molybdenum-depleted zones created by the ordering reaction and described earlier. An example illustrating the variation in the corrosion rate with ageing time at a temperature in the above range (700° C) is given in Fig. 13. Also shown in Fig. 13 are characteristic optical microstructures of corrosion-tested samples in the disordered (annealed) and ordered (aged 100 h at 700° C) states. In the disordered state, corrosion can be seen to have occurred uniformly; however, in the ordered state, extensive intergranular attack was observed. Intergranular attack was, however, more pronounced either after relatively short ageing times at lower temperatures or after longer ageing times at higher temperatures. Such behaviour could be correlated with the discontinuous ordering reaction at the grain boundaries and the associated molybdenum-depleted zones as described earlier.

Table V summarizes the stress corrosion cracking resistance typical of specimens aged 2 and 100 h at 700° C, i.e. ordered to discrete particles and platelets

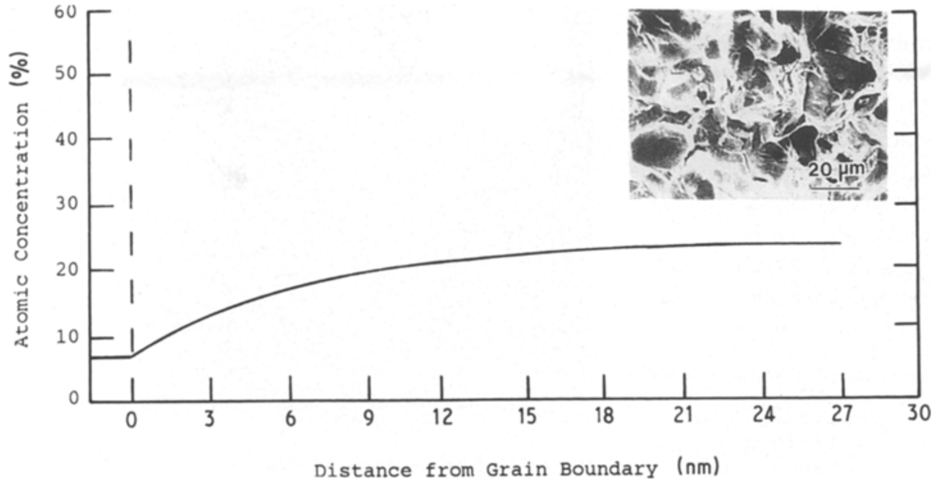

Figure 9 Molybdenum depth profile (concentration against distance from a grain boundary) obtained by Auger electron spectroscopy for a specimen aged 100 h at 700° C. The inset shows the surface of as-fractured specimen inside a scanning Auger microprobe.

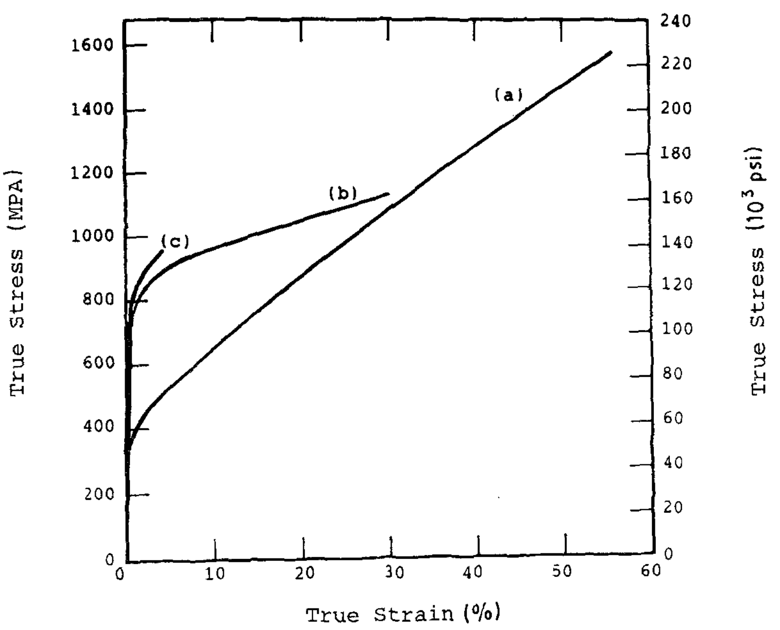

Figure 10 True tensile stress–strain curves derived at room temperature illustrating the effect of long-range ordering on tensile properties. (a) Annealed (disordered). (b) Aged 2 h at 700° C (ordered to discrete particles of Ni_4Mo, Fig. 2b). (c) Aged 100 h at 700° C (ordered to platelets of Ni_4Mo, Fig. 2e).

of Ni_4Mo, respectively. As indicated by the deformation substructures of Fig. 11, the corresponding stacking-fault energy was relatively low. Thus, the higher susceptibility to stress corrosion cracking in the ordered state (Table V) as compared to the disordered state (Table II) could be correlated with a lower stacking-fault energy in the ordered state.

4. Conclusions

The effect of long-range ordering to Ni_4Mo on the corrosion properties of an Ni–Mo alloy was examined. It was found that the ordering reaction degraded the chemical stability of the alloy in reducing media. Deleterious effects of ordering were found to originate from: (i) creation of molybdenum-depleted zones both in the matrix and alongside grain boundaries which had the effect of accelerating the corrosion rate and promoting intergranular attack, and (ii) lowering of the stacking-fault energy which increased the susceptibility to stress corrosion cracking. It was concluded that the corrosion properties of the alloy are far better in the disordered state.

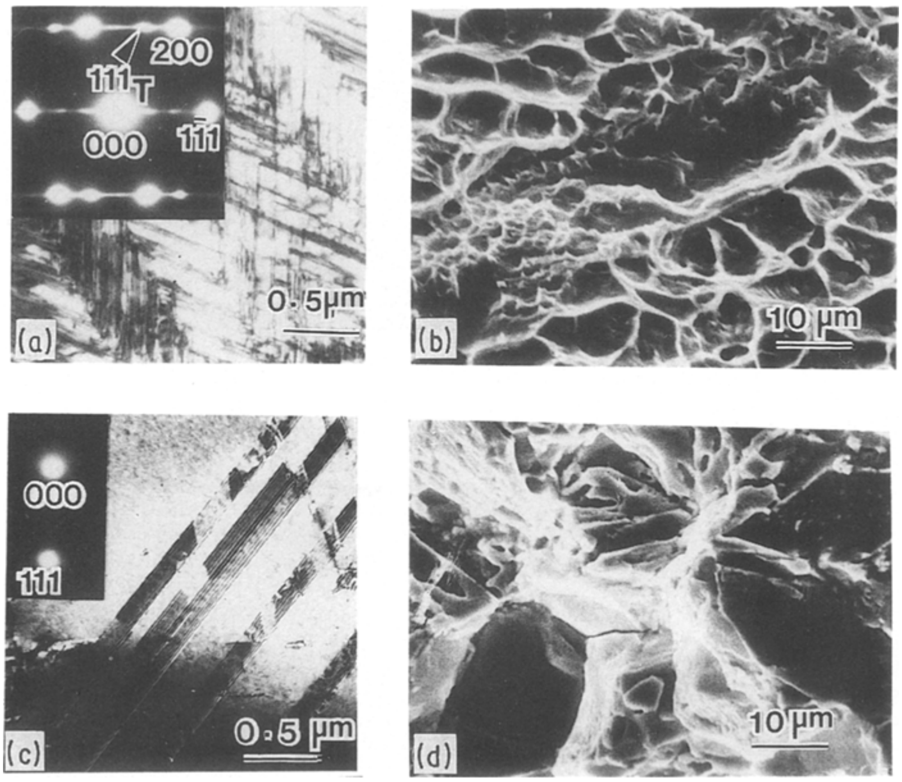

Figure 11 Effect of long-range ordering to Ni_4Mo on the plastic deformation modes and tensile fracture characteristics. (a) Bright-field TEM image and corresponding SAD pattern in [1 1 0] orientation illustrating {1 1 1} deformation twins in a specimen aged 2 h at 700° C and then given 15% elongation. (b) SEM fractograph of the specimen in (a) illustrating a transgranular fracture mode (dimple-type rupture) when Ni_4Mo assumes a discrete-particle morphology. (c) Bright-field TEM image and corresponding SAD pattern in two-beam condition ($g \equiv \langle 1\,1\,1 \rangle$), illustrating {1 1 1} stacking fault in a specimen aged 100 h at 700° C and then given 2% elongation. (d) SEM fractograph of the specimen in (c) illustrating an intergranular fracture mode when Ni_4Mo assume a platelet-type morphology.

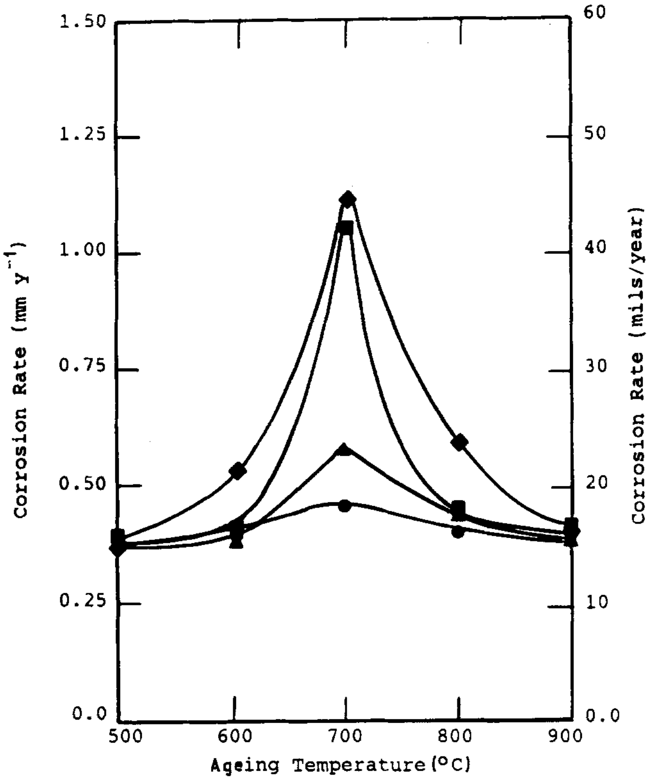

Figure 12 Effect of ageing temperatures (500 to 900° C) and times at a temperature (● 15 min, ▲, 30 min, ■ 1 h, ◆ 2 h) on the corrosion rate in boiling 20% HCl.

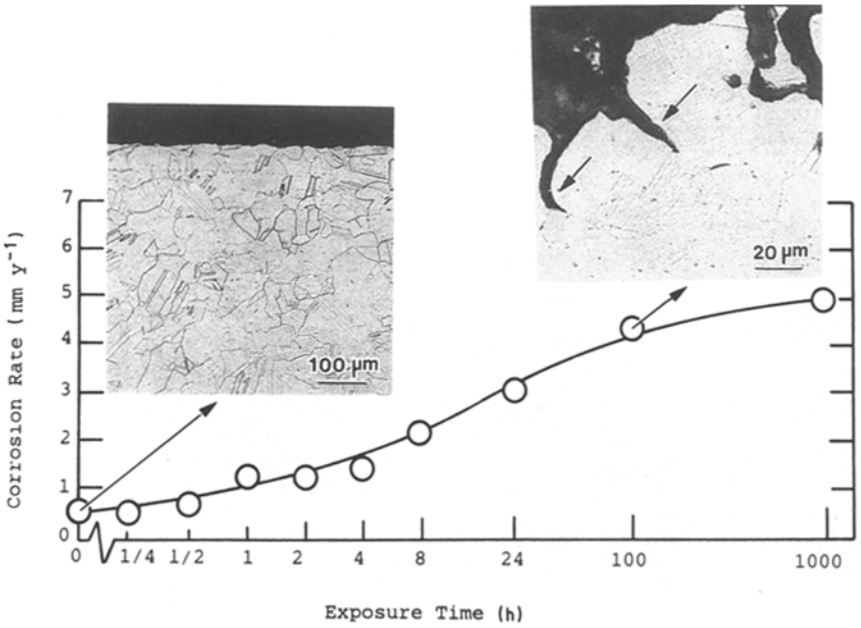

Figure 13 Effect of ageing time at 700° C on the corrosion rate in boiling 20% HCl. The insets are light optical micrographs of corrosion-tested samples as indicated.

Acknowledgements

The support of the Research Institute, King Fahd University of Petroleum and minerals, and permission to publish this work are greatly appreciated.

References

1. WAYNE Z. FRIEND, "Corrosion of Nickel and Nickel-Base Alloy" (Wiley, New York, 1980) p. 248.
2. J. KOLTS, J. B. C. WU and A. I. ASPHAHANI, *Metal Progr.* September (1983) 25.
3. F. G. HODGE and R. W. KIRCHNER, *Mater. Performance* **15** (1976) 40.
4. N. S. STOLOFF, *Int. Met. Rev.* **29** (3) (1984) 123.
5. C. T. LIU, *ibid.* **29** (3) (1984) 168.
6. H. M. TAWANCY and A. I. ASPHAHANI, in "High temperature Ordered Alloys and Intermetallic Compounds", Vol. 39, edited by C. C. Koch, C. T. Liu and N. S. Stoloff (Materials Research Society, Boston, 1985) p. 455.
7. H. M. TAWANCY and M. O. ABOELFOTOH, *Phys. Status Solidi* (*a*) **99** (1987) 461.
8. H. M. TAWANCY, *Scripta Metall.* **18** (1984) 343.
9. C. R. BROOKS, J. E. SPRUIELL and E. E. STANSBURY, *Int. Met. Rev.* **29** (3) (1984) 210.
10. H. L. LOGAN, "The Stress Corrosion of Metals" (Wiley, New York, 1966) p. 178.
11. D. L. DOUGLASS, G. THOMAS and W. R. ROSEY, *Corrosion* **20** (1) (1964) 15t.
12. P. S. KOTVAL, *Metallogr.* **1** (1969) 251.
13. P. J. FILLINGHAM, H. J. LEAMY and L. E. TANNER, in "Electron Microscopy and Structure of Materials", edited by G. Thomas, R. Fulrath and R. M. Fisher (University of California Press, Berkeley, 1972) p. 163.
14. G. THOMAS, *J. Metals*, February (1977) 31.
15. J. I. GOLDSTEIN, in "Introduction to Analytical Electron Microscopy" (Plenum, New York, 1979) p. 83.
16. L. A. NESBIT and D. E. LAUGHLIN, *Acta Metall.* **28** (1980) 989.

Received 28 March
and accepted 1 August 1988